Precursor Chemistry of Lead Bromide Perovskite Nanocrystals

Jakob C. Dahl,[†,‡,¶] Ethan Curling,[†,‡] Matthias Loipersberger,[†] Jason J. Calvin,[†,‡]
Martin Head-Gordon,[†,§] Emory M. Chan,[¶] and A. Paul Alivisatos[∗,†,‖,‡,⊥,#]

†*Department of Chemistry, University of California, Berkeley, California 94720, United States*

‡*Materials Sciences Division, Lawrence Berkeley National Laboratory, Berkeley, California 94720, United States*

¶*Molecular Foundry, Lawrence Berkeley National Laboratory, Berkeley, California 94720, United States*

§ *Chemical Sciences Division, Lawrence Berkeley National Laboratory, Berkeley, CA 94720, USA*

‖*Department of Materials Science and Engineering, University of California, Berkeley, California 94720, United States*

⊥*Kavli Energy NanoScience Institute, Berkeley, California 94720, United States*

#*Current Affiliation: Department of Chemistry, University of Chicago, Chicago, Illinois 60637, United States*

E-mail: paul.alivisatos@uchicago.edu

Abstract

We investigate the early stages of cesium lead bromide perovskite formation through absorption spectroscopy of stopped flow reactions, high-throughput mapping and direct synthesis and titration of potential precursor species. Calorimetric and spectro-

https://doi.org/10.26434/chemrxiv-2024-m6z37 **ORCID:** https://orcid.org/0000-0002-1443-8877

scopic measurements of lead bromide complex titrations combined with theoretical calculations suggest that bromide complexes with higher coordination numbers than previously considered for non-polar systems can better explain observed behaviors. Synthesis mapping of binary lead halides reveals multiple lead bromide species with absorption peaks higher than 300 nm, including a previously observed species with a peak at 313 nm and two species with peaks at 345 and 370 nm that also appear as reaction intermediates during formation of lead bromide perovskites. Based on theoretical calculations of excitonic energies that match within 50 meV, we give a preliminary assignment of these species as two dimensional magic sized clusters with side lengths of 2, 3 and 4 unit cells. Kinetic measurements of the conversion of benzoyl bromide precursor are connected to stopped flow measurements of product formation and demonstrate that the formation of complexes and magic sized clusters (i.e. nucleation) is controlled by precursor decomposition, whereas the growth rate of 2D and 3D perovskites is significantly slower.

Keywords

kinetics, nanoparticles, perovskite, lead bromide, precursors, magic sized clusters, *in-situ* observation

Lead halide perovskites are a class of materials with widespread applications in solar cells,[1] light-emitting diodes,[2] lasers[3] and other optoelectronic devices.[4] Nanocrystals of these materials with quantum yields approaching unity have been created through post-synthetic treatment or synthesized directly. This high quantum yield[5,6] also facilitates novel applications in quantum information[7] and collective luminescence.[8] However, the reactions leading to perovskite nanocrystal formation are not well understood, which impedes the development of next-generation materials with higher stability and structural control.[9] Connecting monomer generation in solution with the formation of nanocrystals has been fundamental to understanding the synthesis process in other systems.[10–12] This understanding has led to a more controlled, rational design of nanomaterial synthesis through tuning of precursor conversion.[13,14]

Equivalent systematic investigations for lead halide perovskites have been challenging.[9] This is due in part to the significantly higher rate of reactions involved - reactions occur over a period of seconds to minutes at low temperatures[15] - especially compared to II-VI or III-V nanocrystal synthesis,[16] which can take hours at elevated temperatures. The ionic nature and ease of phase transformation[17–20] of halide perovskites increase the difficulty of understanding the synthesis process. In addition, the species that is added to the growing nanocrystal, the lead halide complex, may have various stoichiometries, may form cluster compounds and may depend on the halide precursor being used. Studies measuring the kinetics of precursor decomposition and determining the effects on downstream reactions are missing in the context of perovskite nanocrystals. A variety of halide precursors have been reported, including aromatic[6,21] and non-aromatic acyl halides,[22,23] silyl halides,[24,25] alkyl halides,[26] α-haloketones[27] and benzyl halides.[28] We choose here to focus on benzoyl bromide as a precursor, as it has has shown particular promise in reliably forming high quality metal halide nanocrystals[6,21] and undergoes reaction at room temperature.

In this work, we combine stopped-flow observations, high-throughput synthesis, titration, theoretical studies and modeling to elucidate the precursor chemistry involved in the synthesis of $CsPbBr_3$ nanocrystals and related species. We investigate four sets of reactions that are required in combination in order to form nanocrystals:

1. Decomposition of organohalide precursors to form halide ions
2. Complexation of halide ions from 1. with lead to form monomer units
3. Combination of monomer units from 2. into nuclei
4. Addition of monomer units from 2. to nuclei from 3. to form nanocrystals

We determine rate constants and rate laws of benzoyl bromide decomposition. Next, we interrogate the formation of lead bromide complexes with multiple titration and theoretical methods and discuss our results within the context of previous literature reports. Potential magic-sized-nanosheet intermediates are found in transient measurements and through high-throughput experimentation at some low-bromide conditions. These intermediates can be synthesized separately without cesium, and may have an effect on steering the reaction cascade towards particular nanocrystalline products. Finally, we utilize stopped flow absorption spectroscopy measurements to show that the formation of metal halide complexes and the appearance of magic-sized-nanosheets is limited in rate by the benzoyl bromide decomposition, while the growth of larger lead bromide and cesium lead bromide species is limited by other processes. Ultimately, understanding the processes involved in synthesis of lead halide perovskite will facilitate the rational design of improved nanocrystals, such as those with greater stability. The lessons learned from investigating the precursor chemistry will further understanding and control over the formation of a broad range of metal halide nanostructures.

Results

Reaction of Benzoyl Bromide

To understand the initiation of the reaction cascade that gives rise to metal halide perovskite nanocrystals, we investigate the decomposition of a model precursor, benzoyl bromide. In this model reaction first reported by Imran et al,[6] benzoyl bromide and oleylamine react to form oleylbenzamide at room temperature, releasing bromide anions to form the nanocrystals as confirmed by NMR (see Figure S5). We observe that benzoyl bromide has a distinctive double peak optical absorption feature at 295 nm and 282 nm, which shifts to 277 and 270 nm when treated with oleylamine (Figure 1 A). Reactions with oleic acid were not observed to occur by absorption spectroscopy within one minute at 30 °C, though they may occur at higher synthesis temperatures (Figure 1 B, blue line). Tracking the decay of the absorption peak at 295 nm allowed us to utilize stopped flow spectroscopy to determine kinetic rates

(Figure 1 B). Rate laws are first order with regards to the concentration of oleylamine and benzoyl bromide, as would be expected from this reaction (Figure 1 C). A rate constant of around 3 mM^{-1} s^{-1} was measured at 30 °C. Adding oleic acid reduced this rate constant to around 2 mM^{-1} s^{-1}, and this value did not substantially change with different ratios of oleic acid to oleylamine (Figure 1 D). While we would expect the rate of benzoyl bromide decomposition to decrease, since protonated amines cannot be utilized for the nucleophilic attacks required for the formation of oleylbenzamide, the fact that there is only a slight decrease suggests that the oleic acid/oleylamine equilibrium is fast enough to not change the rate substantially (for more information on the oleic acid/oleylamine equilibrium see Figure S1). We thus find the rate equation under the influence of oleic acid at 30 °C to be:

$$\frac{d[BnzBr]}{dt}|_{OA,30°C} = 1.8 \pm 0.4mM^{-1}s^{-1}[BnzBr][OLA] \tag{1}$$

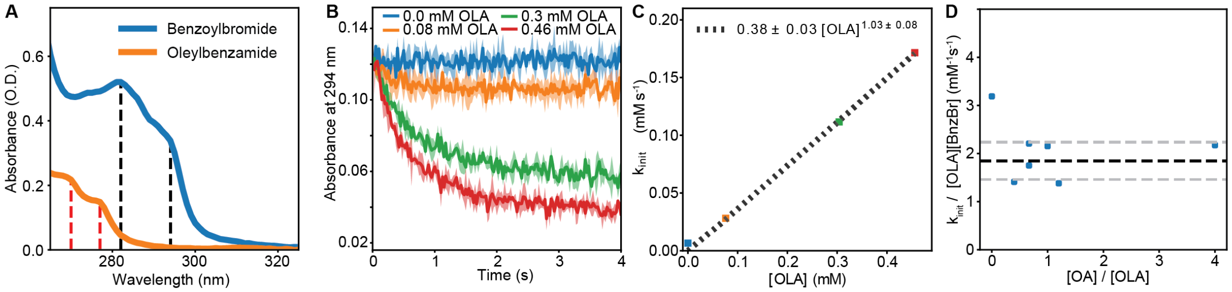

Figure 1: *Reaction of Benzoyl Bromide* A) Spectra of benzoyl bromide and oleylbenzamide, at a nominal concentration of 0.5 mM B) Stopped flow data of changes to the the absorbance at 294 nm with time. C) Calculated rate constant as a function of OA/OLA ratio D) Variation of calculated rate constant with Oleic Acid / Oleylamine Ratio

Lead Bromide Complexation

After precursor decomposition releases bromide ions into solution, the bromide ions must form complexes with lead to form monomer units which can then react to nucleate and grow nanocrystals. To gain insight into the complexation equilibria between the lead bromide complexes and lead species with no bromide complexation, we titrated lead oleate -

https://doi.org/10.26434/chemrxiv-2024-m6z37 **ORCID:** https://orcid.org/0000-0002-1443-8877

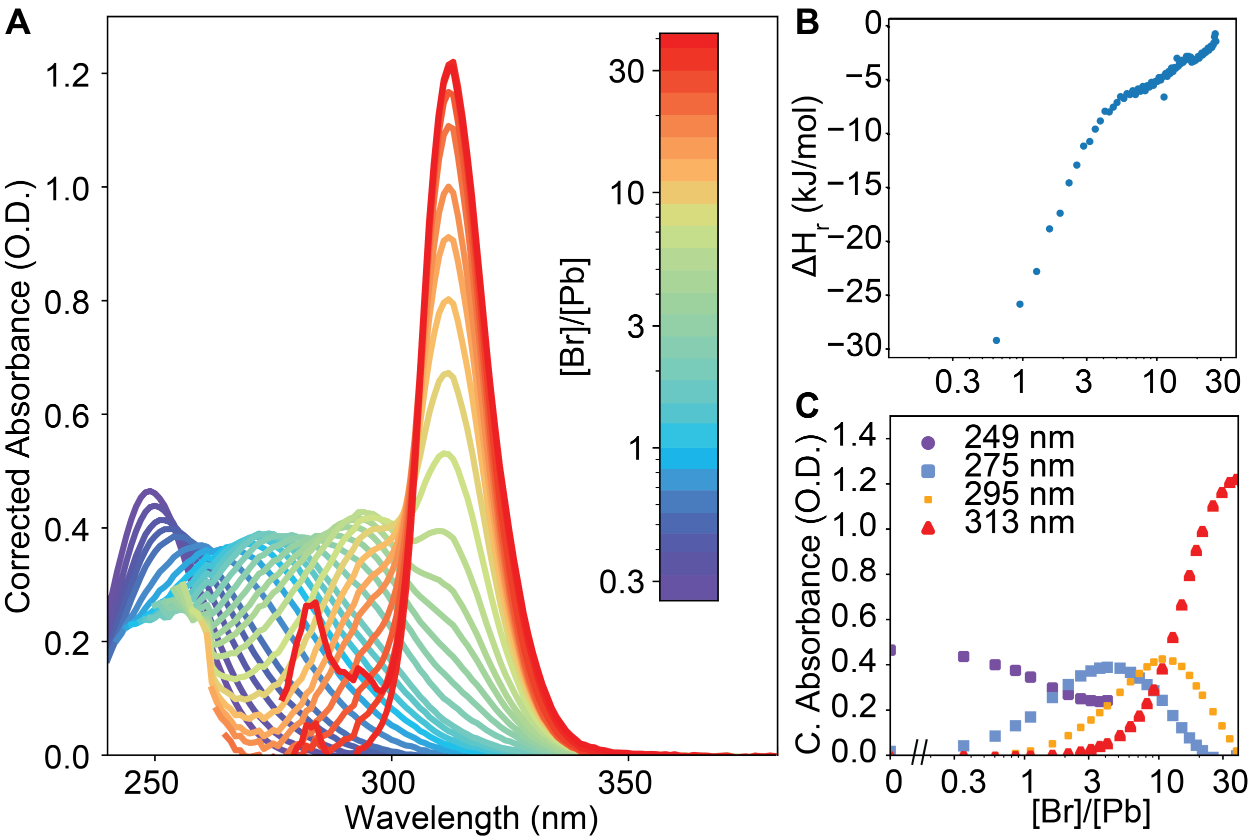

Figure 2: *Titration Data* A) Background corrected absorption spectra of bromide titration into lead oleate B) Reaction enthalpy measured by isothermal titration calorimetry of bromide titration into lead oleate. C) Change of the absorbance of several peaks observed in panel A) as a function of bromide equivalents added

oleylamine solutions with oleylammonium bromide while observing changes in absorption spectral features. With no bromide added, a lead oleate complex shows an absorption peak at around 250 nm (Figure 2 A, leftmost purple line). Addition of oleylammonium bromide generated *in-situ* gradually causes a red-shift, with the addition of six equivalents of bromide leading to a peak at 295-300 nm. Further addition of bromide then leads to the formation of the previously identified species with the characteristic absorption peak at around 313 nm, which saturates at around 30 bromide equivalents. A high oleylamine to lead ratio was required in order to prevent formation of species with absorption features above 313 nm (Figure S2).

From isothermal titration calorimetry (ITC), we can gain a sense of reaction progress by directly measuring the reaction enthalpy (2 B). There is a strong exothermic signal during the initial addition of oleylammonium bromide, reaching up to -30 kJ per mole oleylammonium bromide added. This signal is reduced quickly upon further addition of oleylammonium bromide to approximately -5 kJ/mol at six equivalents of bromide, and then decays down close to baseline at the end of the titration (around 28 bromide equivalents). Isothermal titration calorimetry in principle allows the determination of the heats of reaction, as well as equilibrium constants and the number of additions to a complex, in carefully controlled environments. Due to the overlap of multiple reactions, the ITC data shown here cannot be interpreted as showing a particular type of reaction. What is clear, though, is that there is a qualitative difference between the reactions occurring within the first 6 equivalents of oleylammonium bromide and the reactions occuring thereafter, corresponding to the formation of the species with the 313 nm peak in the optical spectrum.

Using the optical absorption data, we tested model equilibria of complexation, including single component lead bromide complexes coordinating between 2 and 6 bromide anions, as well as dimers forming from 3,4 and 5 coordinated complexes. We chose these models because they allow us to compare the fit of models proposed in literature (formation of $PbBr_3^-$) with the possible models given by further complexation of more bromide ions up

to the octahedral coordination observed in halide perovskite crystal structures (formation of $PbBr_6^{4-}$). We add the possibility of dimer formation to account for small cluster formation.
2Br : $Pb^{2+} + 2Br^- \overset{K_1}{\rightleftharpoons} PbBr^+ + Br^- \overset{K_2}{\rightleftharpoons} PbBr_2$
3Br : $Pb^{2+} + 3Br^- \overset{K_1}{\rightleftharpoons} PbBr^+ + 2Br^- \overset{K_2}{\rightleftharpoons} PbBr_2 + Br^- \overset{K_3}{\rightleftharpoons} PbBr_3^-$
4Br : $Pb^{2+} + 4Br^- \overset{K_1}{\rightleftharpoons} PbBr^+ + 3Br^- \overset{K_2}{\rightleftharpoons} PbBr_2 + 2Br^- \overset{K_3}{\rightleftharpoons} PbBr_3^- + Br^- \overset{K_4}{\rightleftharpoons} PbBr_4^{-2}$
5Br : $Pb^{2+} + 5Br^- \overset{K_1}{\rightleftharpoons} PbBr^+ + 4Br^- \overset{K_2}{\rightleftharpoons} PbBr_2 + 3Br^- \overset{K_3}{\rightleftharpoons} PbBr_3^- + 2Br^- \overset{K_4}{\rightleftharpoons} PbBr_4^{-2} + Br^- \overset{K_5}{\rightleftharpoons} PbBr_5^{-3}$
6Br : $Pb^{2+} + 6Br^- \overset{K_1}{\rightleftharpoons} PbBr^+ + 5Br^- \overset{K_2}{\rightleftharpoons} PbBr_2 + 4Br^- \overset{K_3}{\rightleftharpoons} PbBr_3^- + 3Br^- \overset{K_4}{\rightleftharpoons} PbBr_4^{-2} + 2Br^- \overset{K_5}{\rightleftharpoons} PbBr_5^{-3} + Br^- \overset{K_6}{\rightleftharpoons} PbBr_6^{-4}$
3Br-Dimer : $2Pb^{2+} + 7Br^- \overset{K_1}{\rightleftharpoons} 2PbBr^+ + 5Br^- \overset{K_2}{\rightleftharpoons} 2PbBr_2 + 3Br^- \overset{K_3}{\rightleftharpoons} 2PbBr_3^- + Br^- \overset{K_D}{\rightleftharpoons} Pb_2Br_7^{-3}$
4Br-Dimer : $2Pb^{2+} + 9Br^- \overset{K_1}{\rightleftharpoons} 2PbBr^+ + 7Br^- \overset{K_2}{\rightleftharpoons} 2PbBr_2 + 5Br^- \overset{K_3}{\rightleftharpoons} 2PbBr_3^- + 3Br^- \overset{K_4}{\rightleftharpoons} 2PbBr_4^{-2} + Br^- \overset{K_D}{\rightleftharpoons} Pb_2Br_9^{-5}$
5Br-Dimer : $2Pb^{2+} + 11Br^- \overset{K_1}{\rightleftharpoons} 2PbBr^+ + 9Br^- \overset{K_2}{\rightleftharpoons} 2PbBr_2 + 7Br^- \overset{K_3}{\rightleftharpoons} 2PbBr_3^- + 5Br^- \overset{K_4}{\rightleftharpoons} 2PbBr_4^{-2} + 3Br^- \overset{K_5}{\rightleftharpoons} 2PbBr_5^{-3} + Br^- \overset{K_D}{\rightleftharpoons} Pb_2Br_{11}^{-7}$

We created a computational method that allowed the fitting of spectra over multiple equilibrium variables. For each model, we optimized the equilibrium constants by simulating the distribution of complexes under a given equilibrium law, fitting the spectra of each species either through linear interpolation and iterative subtraction of defined spectra or through linear regression of each wavelength to generate an extinction spectrum, and finally determining the resulting overall fit to the titration data. We have found that fits using iterative linear decomposition of spectra resulted in more realistic predicted spectra of the different lead bromide species (Figure 3 D) and lower errors in reproducing experimental data compared to multivariable linear regression. By comparing the residuals of different methods, we can attempt to understand which models give reasonable approximations of the observed data (Figure 3 A). In this case, the models **5Br**, **6Br** and **5Br-Dimer** are roughly equivalent and have roughly half the observed error of the next best equilibrium models.

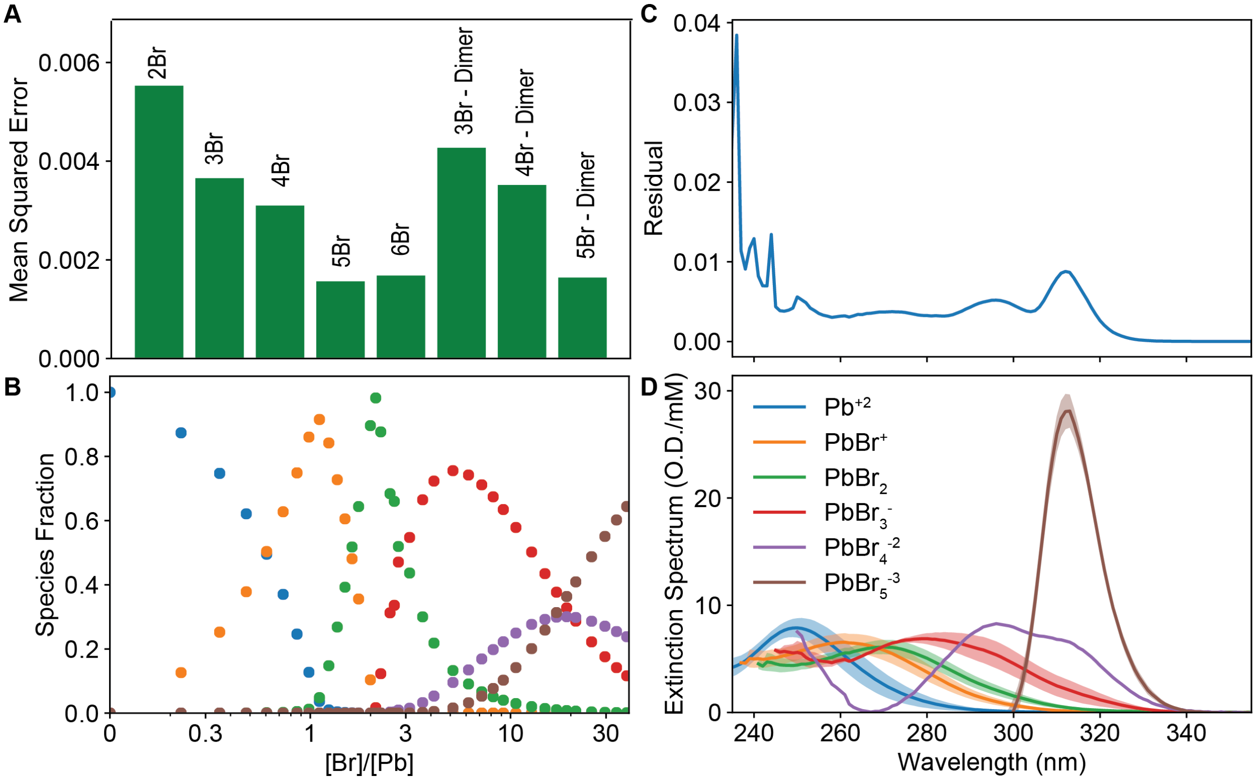

Figure 3: *Analysis of* $PbBr_x$ *Complex Titration Data* A) Mean squared error for different models tested. B) Simulated concentrations of species from the best performing model in (A), 5Br, at points at which the measurements were conducted. Colors are the same as those used for the extinction spectra in D. C) Residual error of each wavelength for 5Br model. D) Calculated extinction spectra for the different species in the 5Br model.

Using DFT calculations, we can gain additional insight into the energetics of the reaction. We generated a manifold of different possible lead complexes coordinated by amine, carboxylate and bromide groups, with ammonium groups present as counterions in a non-polar dielectric medium with $\varepsilon_{rel} = 2$. For each $PbBr_x$ combination, we identify the complex with the lowest Gibbs formation energy. We observe that lead complexes binding up to two amine groups are stabilized by 12 - 24 kJ/mol relative to complexes without binding amine groups, and binding more than two amine groups appears generally to destabilize the complex, regardless of coordination number. Complexes with coordination numbers above six frequently decompose during geometry relaxation, so we do not consider them here. By

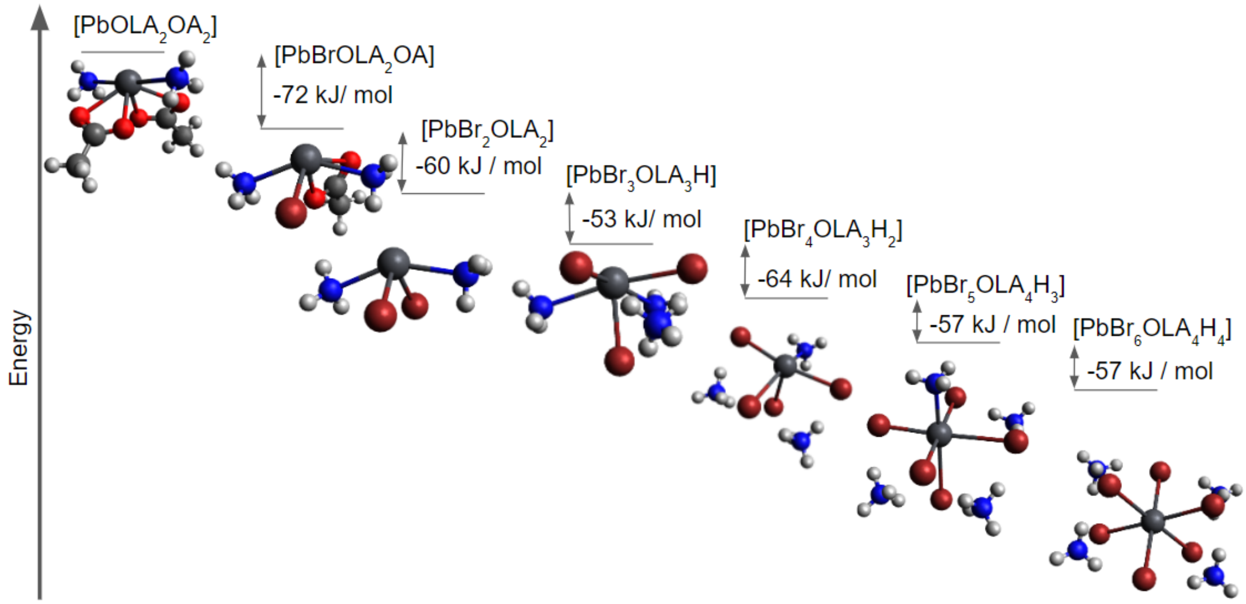

Figure 4: *DFT Structures and Energies of Lead Bromide Complexes* Dark grey: Pb; Blue N; white H; red O; light grey: C

using ammonium bromide as an uncharged addition agent, we can then analyze the Gibbs energy of reaction for each bromide addition. This energy is quite negative for each addition up to $PbBr_6^{4-}$, at around 50 - 70 kJ/mol per additional bromide added. This suggests that equilibria of lead binding more bromide counterions are highly favourable beyond three bromide ions - which is reasonable from hard-soft acid-base theory, in which lead and bromide ions are well matched.[29] The favourable binding also matches experimental observations in aqueous solution measuring bromide ion concentrations, which report $PbBr_7^{5-}$ as the complex at high bromide concentrations.[30] We also note that forming dimers appears generally favourable as well, in line with previous observations of multinuclear complexes.[31]

Potential Magic-Sized Cluster Intermediates

After monomer units have formed, the next step in the formation of nanocrystals is nucleation. We use high-throughput synthesis and analysis routines we established previously[20] to further probe the synthesis of lead bromide at varied concentrations of oleylamine and bro-

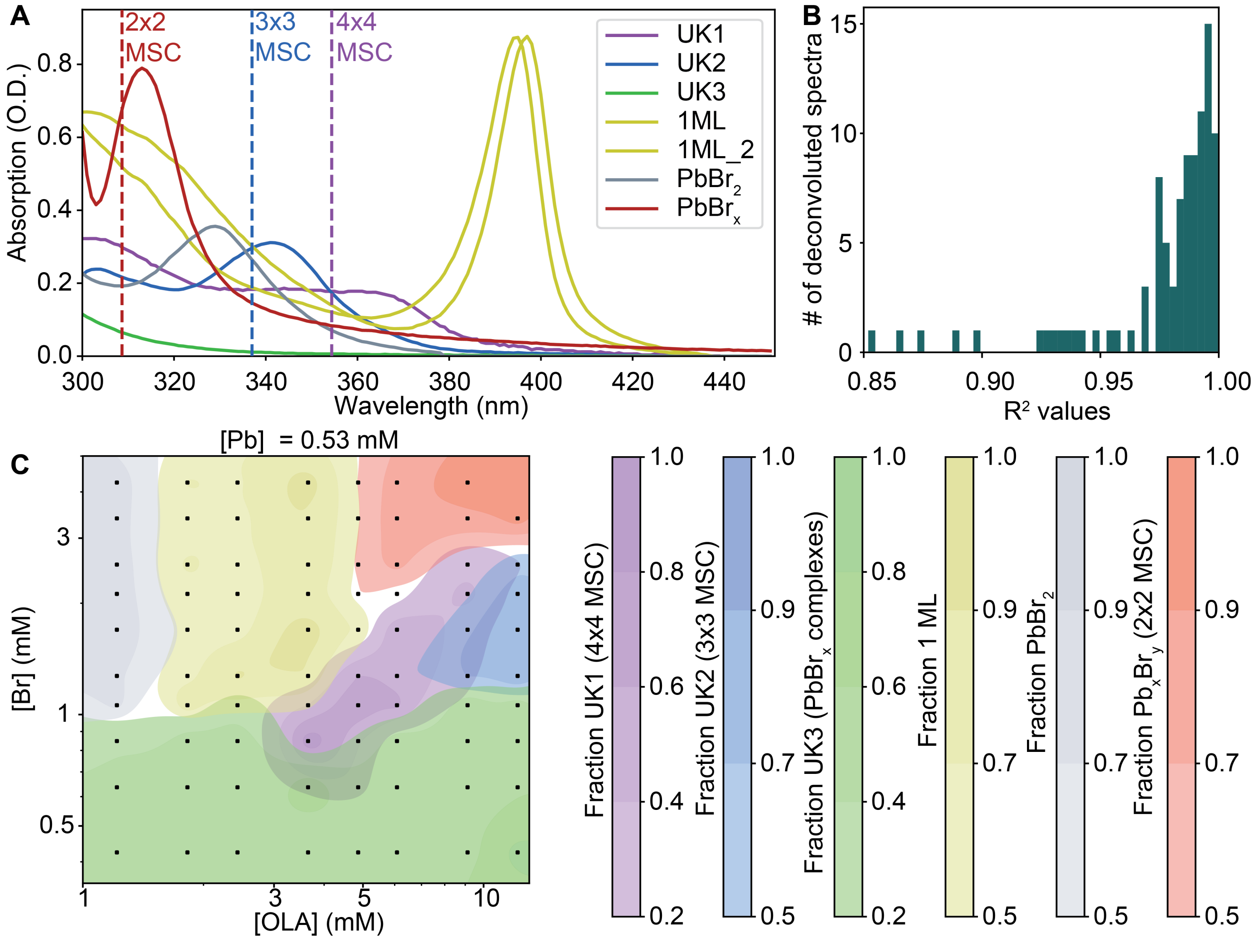

Figure 5: *High Throughput Synthesis at low Br : Pb ratios* A) Spectra used to analyze the synthesis. Dotted lines depict theoretically predicted exciton peak values of 2x2, 3x3 and 4x4 square nanosheets of OLA$_2$PbBr$_4$ composition.[32] B) R^2 values of high-throughput spectra. C) Map of product distribution as a function of bromide and oleylamine concentration.

mide (Figure 5 C) in search of potential intermediate clusters. This factorial search showed that the three main binary lead halide products previously identified - $PbBr_2$ nanocrystals, 2-D OLA_2PbBr_4 nanosheets, and the lead bromide complex absorbing at 313 nm - are the main products of this reaction at $Br : Pb > 6$. Below this ratio, other products may appear. Using the previously developed deconvolution algorithm[20] and manually adding new reference spectra (Figure 5 A) until the collection of spectra is well described (Figure 5 B), these unknown products (UK1, UK2, UK3) can be grouped into species with three distinct absorption features: 1) species with rising absorption band starting at around 310-330 nm (UK1), 2) species with a broad peak around 360-370 nm (UK2), 3) species with a peak around 345 nm (UK3). UK1 looks visually similar to the products in the lead oleate titration and likely corresponds to lead bromide complexes with a single lead atom, though we cannot perform our previous optical analysis to figure out which coordination number is most likely due to noise in the spectrum below 300 nm. At low OLA : Pb ratios, this product is adjacent to $PbBr_2$ nanocrystals at a Br : Pb ratio of around 2, as would be expected stoichiometrically. Surprisingly, the transition to OLA_2PbBr_4 can also occur at this stoichiometry at slightly higher OLA:Pb ratios - likely the result of a transformation process from $PbBr_2$ nanocrystals observed previously[20,33] and investigated in detail elsewhere.[32] At higher OLA : Pb ratios, the second (370 nm) species appears at bromide concentrations between the 2 D perovskite nanosheet and the first species. The point at which OLA_2PbBr_4, and the species UK2 form then shifts gradually to a Pb : Br ratio of 4 : 1 as the OLA to Pb ratio increases. Species UK3 (345 nm) occurs primarily between the 313 nm product and the lead bromide complexes, at a Pb:Br ratio above 4:1. Based on the results of the titration experiments, it appears unlikely that products 2 and 3 are complexes with a single lead atom. Based on comparisons to theoretical calculations,[32] the species at 345 and 370 nm may be assigned to a two dimensional perovskite 3x3 or 4x4 unit cell plate, respectively - the error to the predicted absorption maximum is only 50 meV. A similar identification of the peak at 313 nm with a 2x2 unit cell plate may also be made. We will use the terms 3x3 and 4x4 magic sized cluster (MSC) hereafter, though we would like to stress that this is a provisional assignment lacking structural characterization, similar to initial assignments made for magic sized clusters in III-V[13] and II-VI[34,35] nanocrystal formation studies. While magic sized clusters usually have very sharp peaks, we believe that the lability of lead halide species may cause them to experience subtle differences in coordination environment, which could easily lead to shifts in the spectra, and thus a broad peak that can change in width and position.

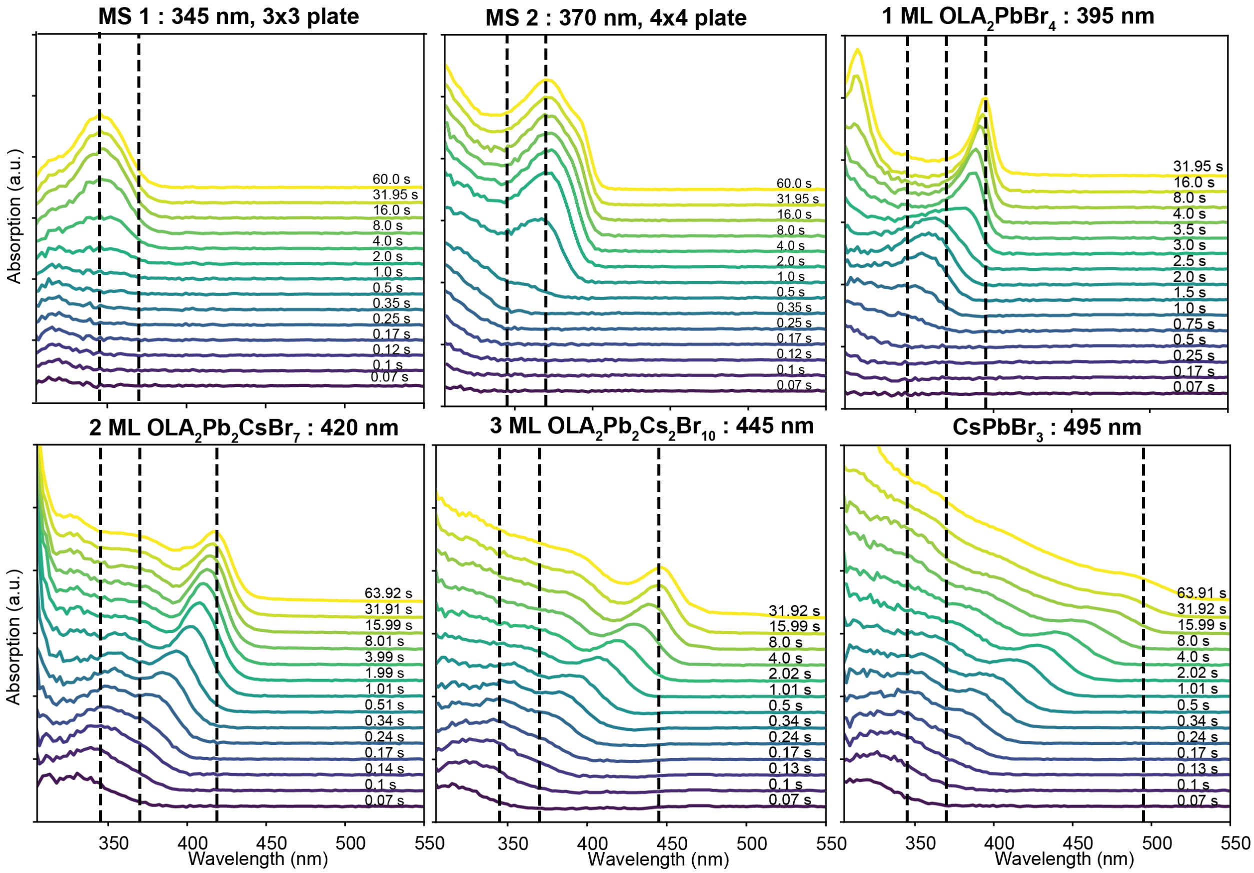

Figure 6: *Kinetic Data with potential Magic Sized Cluster Intermediates* The stacked plots correspond to absorption spectra taken during the reaction at logarithmic time intervals, with the bottom corresponding to the beginning of the reaction and the top corresponding to the end of the reaction. Dashed vertical lines are placed in the plots to guide the eye towards 345 nm (MS 1, 345 nm, 3x3 plate), 370 nm (MS 2: 370 nm, 4x4 plate) as well as the final species formed.

We were also able to observe the formation of the potential 3x3 and 4x4 MSCs using stopped flow absorption spectroscopy (Figure 6). Both of these species appear at 0.5 - 1 s after a species with an absorption edge starting around 340 nm is formed, which is most likely $PbBr_3$ or $PbBr_4$ based on our titration analysis. We further observed that species with 345 and 370 nm absorption features occur during the formation of different products. Most obviously, the formation of single layer nanosheets through direct nucleation will generally form a species with an absorption spectrum at 370 nm. This species is longer lived at higher olelyamine concentrations and lower temperatures, where a rather sudden transition to larger species can be observed. A species with an absorption peak at 345 nm is clearly present in synthesis of 2 and 3 layer thick nanoplatelets as well as in some synthesis of nanocubes. There appears to be a transition to a species with a peak around 380 nm, which could itself be a magic sized cluster containing cesium, perhaps a smaller version of the 399 nm species identified previously.[36] This species then shifts in wavelength continuously until the final product is reached. We have also synthesized larger quantities of these clusters which are stable at room temperature and under open atmosphere for several hours. Attempting to transform these species with cesium oleate reveals that the 370 nm (4x4 MSC) species transforms mostly to monolayer nanosheets with a peak at around 395 nm and only gradually transforms into larger species (Figure S6). These observations suggest that the 370 nm (4x4 MSC) and 345 nm (3x3 MSC) species may be involved in differentiating pathways towards different products.

Effect of Bromide Precursor Conversion on Reaction Kinetics

Using the same stopped flow data, we can also analyze the effect that the release of bromide ions has on the formation of different species, illustrating which part of the nanocrystal synthesis reaction network is controlled by precursor reactivity. We calculate the amount of bromide released over time based on the initial conditions of the reaction and the 2nd order rate law determined in equation (1). We then compare this release of bromide ions to the formation of different species in solution by observing their relative absorbance at 313

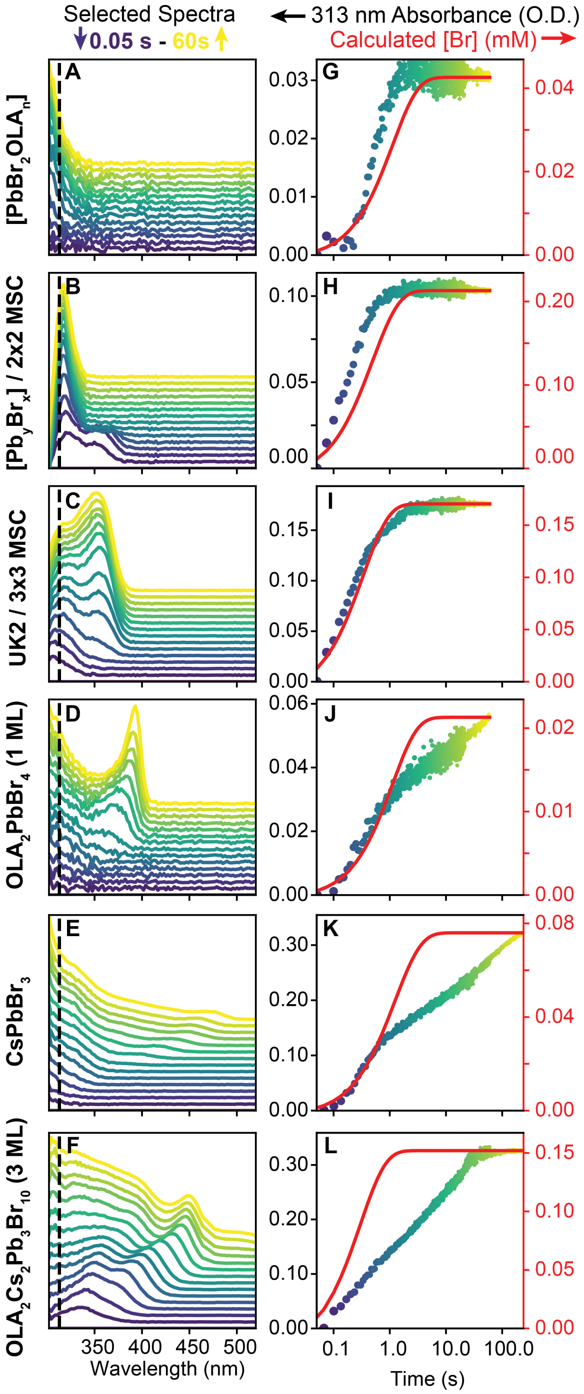

Figure 7: *Influence of Bromide Conversion Kinetics on Species Formation Rates* A-F Selected spectra of species formation; G-L simulated release of bromide compared to change in absorbance at 313 nm over time. A and G: $PbBr_2$ complex (Br:Pb ratio ~ 2), B and H: Pb_xBr_y complex (2x2 MSC, Br:Pb ratio ~ 16), C and I: potential 3x3 MSC, D and J: OLA_2PbBr_4 (1 ML), E and K: $CsPbBr_3$ (Cesium lead bromide perovskite), F and L: $OLA_2Cs_2Pb_3Br_{10}$ (3 ML),

nm, a wavelength at which virtually all lead bromide species absorb light and that is high enough above the band gaps of all but one of the clusters we have identified that it is likely to scale most directly with the number of lead bromide unit cells. By comparing the calculated bromide concentration against the measured absorbance values, we get a sense of what parts of the synthesis process are limited by the decomposition of the precursor and thus follow the trend given by the calculated bromide concentration, and which parts are limited by other processes and lag significantly behind the release of bromide. As we can see in Figure 7 G, H and I, the bromide complexes (G) as well as the potential magic sized clusters (H and I) follow the calculated bromide concentration curve. Lead bromide complexation and formation of small lead-bromide nanosheet nuclei thus proceed at a rate that is faster than the reaction of benzoyl bromide with oleylamine. However, this does not appear to hold true for larger species: single layer OLA_2PbBr_4, three layer $OLA_2Cs_2Pb_3Br_{10}$, and $CsPbBr_3$ nanocrystals. All of these initially follow the curve given by the bromide concentration but then proceed more slowly once initial nuclei are formed after $\sim 0.1 - 1$ s.

Discussion

Our investigation into the decomposition of benzoyl bromide (Figure 8 A) showcases that the precursor decomposition kinetics that are crucial for II-VI and III-V nanocrystals are similarly important for metal halide nanocrystals. In principle, different acyl halides and similar compounds may provide a platform for synthesis modulation of perovskite nanocrystals in a fashion analogous to the thiourea compounds developed for II-VI nanocrystals.[14,37]

Another important result of this study is improved understanding of the lead bromide complexes in solution (Figure 8 B). Previously, lead bromide complexes with a peak wavelength of approximately 313 nm have been identified as $[PbBr_3^-]$ due to their spectral similarity to complexes in acetonitrile[38] and equilibria observed in dimethylformamide.[39] However, spectra of complexes can shift due to different solvent and coordination environ-

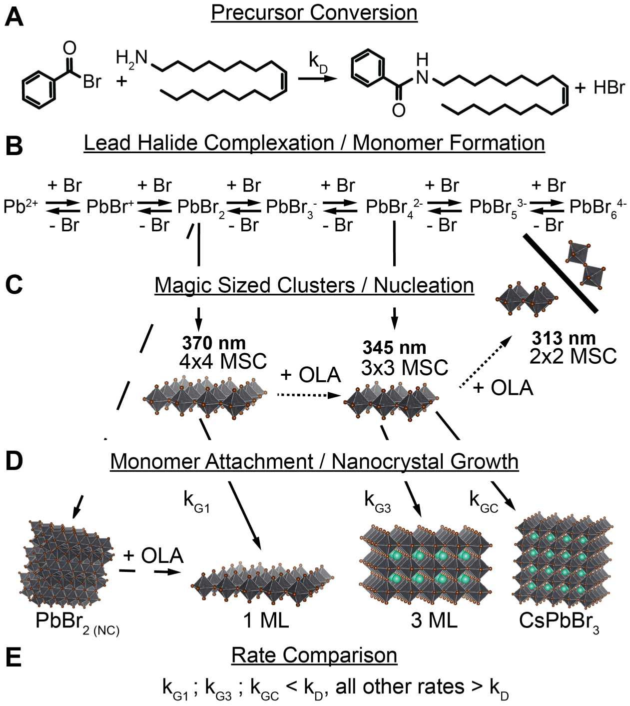

Figure 8: Reaction scheme detailing the species investigated here, their relationships to each other and function in the synthesis. A) Benzoyl bromide conversion to halide ions, B) complexation of lead with bromide ions, C) Potential magic sized cluster intermediates, D) Nanocrystalline products, E) comparison of rate constants. Solid lines denote reactions investigated here, dashed lines denote reactions that have been investigated in detail previously,[32] dotted lines are placed in analogy to similar transformations of all of the shown perovskite nanocrystal species (1 ML, 3 ML, $CsPbBr_3$) to the species absorbing at 313 nm under addition of OLA.[17,18,20]

ments(acetonitrile,[38] propylene carbonate,[31] reverse micelles[40] and water[30]). In addition, this identification contrasts with lead iodide chemistry, where X-ray absorption spectroscopy suggested hexacoordinated lead iodide complexes in dimethylformamide,[41] and where several hexacoordinated cluster species have been isolated as solids.[42–45]

Our work combining experimental observations and theory suggest that single center coordination complexes of $PbBr_3^-$ are unlikely to be the species absorbing at 313 nm and play an important role in the chemistry of perovskite nanocrystals in apolar solution for the following reasons:

1. DFT calculations do not show significant differences in the Gibbs enthalpy of reaction for addition of bromides to lead bromide complexes with different numbers of coordinated bromides.
2. Absorption spectra of a titration series are only poorly described by complexation equilibria with fewer than 5 or 6 coordinated bromides, or multinuclear clusters.
3. The extinction of the species at 313 nm itself is around threefold higher than that of the lead bromide species at lower bromide concentrations, which suggests a significant change to the coordination environment.

We find a compound with multiple lead centers to be the most likely answer based on our own results and given the observation of such compounds in lead iodide solutions in more polar solvents. The use of non-polar solvents should reduce stabilization of a charged complex in solution and the substitution of bromide for iodide should further decrease the delocalization of charge. Both changes make it more likely to observe a complex with multiple lead atoms in which charged atoms interact more with each other than with the surrounding environment. In addition, nanocrystalline intermediates and products appear at a range of bromide equivalents that can require at most a particular number of coordinated bromides in the lead bromide complexes acting as monomer units, ranging from 2 equivalents for $PbBr_2$, OLA_2PbBr_4 and 370 nm species (4x4 MSCs) to 4 equivalents for 345 nm species (3x3

MSCs) and ≥ 6 equivalents for the 313 nm species (2x2 MSCs or other $\mathrm{Pb}_x\mathrm{Br}_y$ clusters) (relationships as shown with arrows between Figure 8 B and C). We give here an initial overview of possibilities we find likely. More research to differentiate these possibilities for lead bromide complexation in polar and non-polar solutions is needed.

Observing the potential role of magic sized nanosheet clusters in the synthesis of perovskite nanocrystals and nanoplates adds additional insight into the formation process of perovskite nanocrystals (Figure 8 C, red box). The observation of the 370 nm cluster in formation of 1 ML nanosheets and the 345 nm cluster in the formation of perovskite nanoplates and nanocrystals suggests that there may even be differentiating pathways between the clusters. The rapidity of transformation of the 370 nm cluster to 1 ML nanosheets and the subsequent slow transformation to thicker nanostructures supports this interpretation. The central position of very small nanosheets in the synthesis of diverse nanoplate and nanoparticle products matches well with previous theory developed for CdSe nanoplatelet formation.[46–48] However, while we have occasionally observed kinetics that are in line with Ostwald ripening between thin and thick nanosheets (Figure S3), our observations suggest that in most cases the formation of nanosheets of the final observed thickness or even a transition to an isotropic shape occurs rapidly while the nanosheets are still small in lateral extent.

Finally, by integrating the precursor conversion of benzoyl bromide with stopped flow measurements of product formation (Figure 8 D), the relative rates of these kinetics could be elucidated (Figure 8 E). Complexation and formation of nuclei are fast - even faster than the decomposition of a reactive agent - while growth proceeds more slowly, even if all reagents have been released into solution. Based on our data, it is unlikely that the major factor impeding growth here is Ostwald ripening of the same species - if this were the case, we would expect to only observe a shift in the peak position of the exciton (change in size) but no change in the absorbance above the bandgap (change in total number of unit cells). That we observe both suggests that it is the attachment of monomers to the nanoparticles themselves that proceeds at a slow rate. This is substantially different from previous work on II-VI nanocrystals where precursor decomposition is the rate limiting step,[10,11,14] and suggests that different approaches to controlling the formation of nanocrystals may be successful, as has been shown recently through equilibrium control by Akkerman and coworkers.[49,50]

Conclusion and Outlook

In this work, we have investigated the precursor chemistry and early reaction kinetics of lead bromide species, including cesium lead bromide perovskites. We determine equilibrium constants for the oleylamine / oleic acid equilibrium based on NMR measurements as well as for lead bromide complexation based on optical and calorimetry measurements. Further, we determine the rate constant of decomposition for benzoyl bromide. We show that current models of lead bromide complexation in non-polar solvents must be expanded to include higher-coordinating and multinuclear lead bromide species to accurately describe existing data, which is further supported by DFT calculations. The extent of bromide excess over lead leads to important changes in the final lead bromide nanoparticle products observed as well, with observation of species that may correspond to 3x3 and 4x4 magic sized nanosheets. We also observe similarly absorbing species in synthesis of single layer lead bromide nanosheets and in perovskite nanocubes and 2 and 3 atomic layer nanoplatelets. We show the effect that bromide release has on all of these species, and find that bromide release is the rate determining step in the formation of lead bromide complexes and the potential magic sized clusters, but that growth of larger nanostructures proceeds slowly through addition of monomer units after the initial nuclei have formed. Together, this work forms the basis of a more nuanced and holistic understanding of the chemistry involved during nucleation and growth of lead bromide perovskites.

This work also highlights possible synthetic targets, such as the potential magic sized cluster species absorbing at 313, 345 and 370 nm that could be used in order to confirm the chemical identity and structure, or suggest changes to the model proposed here. Our work suggests that the reaction pathways of metal halide nanocrystals can be manipulated through further development of halide precursors, to expand their libraries and tune their reaction dynamics. Overall, we develop insight into the cascade of reactions important for perovskite nanocrystal formation. Understanding the fundamental solution chemistry involved in forming these complex nanocrystals will be crucial to more rational control over metal halide nanocrystal synthesis and their properties.

Experimental

Materials

Dodecane (>99.0%), lead acetate ($Pb(CH_3COO)_2$, >97.0%), oleylamine (OLA) ≥99.0%), cesium acetate (99%), oleic acid (OA) ≥99.0%) and benzoyl bromide ≥99.0%) were purchased from Sigma Aldrich. Hexane (mixed isomers, 98 %) was purchased from Fischer Scientific. All materials were used as received.

Nuclear Magnetic Resonance Spectroscopy

In a 1 mL NMR tube, 15 μ L of oleylamine were added to 500 μ L of Toluene. ^{1}H NMR measurements were performed on a 400 MHz Bruker AVB Spectrometer. After each measurement, more oleic acid was titrated into the mixture, and the measurement repeated.

UV-VIS Titration of Lead Oleate

Lead oleate was prepared as described previously.[20,51] 3 μ L of lead oleate solution, 40 μ L oleylamine and 20 μ L oleic acid were added to 4 mL of hexane. 300 μ L of this solution were diluted into 2 mL in a quartz glass cuvette for a final lead concentration of 0.065 mM. A benzoyl bromide titration solution was prepared by mixing 3 μ L of benzoyl bromide with 2 mL of hexane for a final solution concentration of 12.6 mM, or 0.084 Pb equivalents of bromide per μ L. This solution was added stepwise to the solution of lead oleate - oleylamine, and absorption measurements were taken between every addition. The reaction was close to instantaneous. A reference sample including the same amount of oleylamine and oleic acid, but no lead oleate was titrated with the same benzoyl bromide solution to measure and subtract the absorbance of organic oleylbenzamide generated during the reaction. Oleylamine and oleic acid were subtracted from all measurements based on the absorption of the reference prior to titration. A linear exctinction value of oleylbenzamide was calculated from titration of the reference solution (see Figure S4), and the calculated absorbance was subtracted from the titrated lead bromide solution. Absorbance values over 1.5 O.D. in raw data measurements were excluded from analysis.

Isothermal Titration Calorimetry of Lead Oleate

Pre-reacted benzoyl bromide solution was prepared by mixing 66 μ L OLA with 33 μ L OA in 10 mL dodecane and adding 13.7 μ L benzoyl bromide and briefly shaking the solution for a final content of 10 mM bromide, 20 mM OLA and 10.4 mM OA. Lead Oleate solution was added by mixing 3 μ L lead oleate solution in OLA (0.66 M Pb content) with 66μ L OLA and 30 μ L OA in 10 mL dodecane for a final content of 0.2 mM lead, 20 mM OLA and 10.4 mM OA. All measurements were performed using a TA Instruments Nano isothermal titration calorimeter (ITC). For measurement, 1.198 ± 0.006 mL of sample solution was placed in the sample cell (effective volume of 965 ± 5 μ L) and 1.198 ± 0.006 mL dodecane was placed in the reference cell with the reference needle. The syringe was loaded with 250 μ L of pre-reacted benzoyl-bromide solution in dodecane. The temperature was maintained at 25 °C through the titration. After stirring was initiated at 250 rpm, the samples were allowed to equilibrate until the differential heating slope was ≤ 0.1 μ W/h and the standard deviation in the differential heating was ≤ 0.01 μ W over a period of lasting $\sim$ 40 min. After equilibration, an initial baseline was taken for 2400 s, and then 2.2 ± 0.2 μ L of titrant solution was injected per injection. Between each injection the solution was stirred for 2400 s to allow the system to return to equilibrium. Integration of titration peaks calculates the heat of reaction. The standard error in the heat of injection is 23 μ J and was determined by injecting water into water. Background subtractions were performed by injecting the ligand solution into a dodecane solution containing equivalent concentrations of oleylamine and oleic acid (20 mM OLA and 10.4 mM OA) in an identical manner to the sample measurements and subtracting the integrated heat from the sample measurements.

DFT Calculations of Lead Halide Complexes

Density functional theory (DFT) calculations for free energies were performed with the Q-Chem package[52](version 5.3.0) using the B3LYP functional[53–55] with a mixed basis for the optimization and frequency calculations (def2-SVP basis for C,H,O, def2-SVPD for N and Br, def2-TZVP basis set for Pb).[56,57] In addition, the def2-ecp was used for Pb throughout[58] and Grimme's D3 correction.[59] Gibbs free energies were computed using the zero-point energy correction and the entropic contribution is calculated from the vibrational frequencies at T = 298 K. Solvation energies were approximated by performing single-point calculations with the implicit solvation model SMD[60] (using dodecane). The electronic structure was refined with the large basis set single point calculations using the def2-TZVPPD basis for all elements.[56,57] A combinatorial set of possible charge neutral lead complexes with amine, carboxylate and ammonium ligation with coordination numbers up to 6 was evaluated for each $PbBr_x$ complex, with x being all integers from 0 to 6, assuming a formal +2 charge of lead. Reaction energies were calculated with respect to charge neutral amine, ammonium bromide and ammonium acetate species in solution. The reaction energies of complexes with a number of bromides were evaluated with regard to the complex with the minimum number of ligands for charge balance. The structures of complexes with the most negative Gibbs free energy of reaction compared to the minimal complex are displayed in Figure 4, and the reaction energies of ammonium bromide addition (and ligand displacement, where applicable) were calculated between successive complexes.

Analysis of Titration Measurements

All absorption spectra in which there was no absorbance above 340 nm was used in the analysis, background subtracted and selected as described above. This data was fit directly to equilibrium constants. First, the chosen equilibrium constants and the titration conditions were used to calculate substance concentrations using chempys equilibrium system solver.[61] Based on these calculated concentrations, for each species we determined the points where only that species and species with a lower coordination number are occuring at fractions above 5%. The extinction spectra were then calculated by iteratively finding, for each species, the points at which no other absorbance should be present, then taking the average of the absorbance values divided by the concentration values at each wavelength, and then subtracting the reference spectra from the rest of the dataset. We constructed a loss function based on the logarithm of the mean-square error of fit to the combined spectra and the average variance in absorbance values of the extinction spectra, combined with a penalty for negative absorption values in the extinction spectra. In cases where it was not possible to determine the spectra, a high value was returned. This function was optimized with respect to the equilibrium constants using active learning with a gradient boosting regression tree surrogate function as implemented in scikit-optimize with bounds for the equilibrium constants between 10^{-2} and 10^{10}, 250 function calls with expected improvement as the acquisition function.

In-situ Stopped Flow Experiments

All stopped flow experiments were performed on an Applied Photophysics SX 20 stopped flow spectrophotometer using a photodiode array with 25 ms integration time for 1000 time points. The stopped flow chambers were stored under ethanol, then filled with toluene and emptied three times, then filled with dodecane and emptied three times before measurement.

Stock solutions of Br, OLA, OA, Cs-OA and Pb-OA were prepared as described previously,[20] but diluted to 8.5 or 0.85, 3.0, 3.2, 1.0 and 0.66 mM in dodecane, respectively. All stock solutions were added to the syringes used for loading the stopped flow chambers with volumes varying between 10 - 100 uL and mixed with dodecane to a final volume of 2 mL. For synthesis experiments, OLA, OA, Cs-OA and Pb-OA solutions were placed in one syringe and Br solutions were placed in the other syringe. Each experiment was performed at least in triplicate for a duration of 60 seconds.

High-Throughput Synthesis and Optical Analysis

For high-throughput synthesis, dodecane solutions of lead oleate (200 x diluted from a Pb-OA stock solution), benzoyl bromide (800 x diluted), oleylamine (100 x diluted) and oleic acid (80 x diluted) were freshly prepared. Using a Hamilton NIMBUS4 Microlab liquid handling robot, dodecane, oleylamine, lead oleate, oleic acid and cesium oleate solutions were added in varying proportions to a 96 well plate equipped with single-use 1 mL glass vials. The entire plate was heated to the reaction temperature while shaking at 300 rpm and kept at the reaction temperature for 800 s. Under continued shaking, benzoyl bromide solution was added to each vial, for a final reaction volume of 500 μ L. This addition sequence was typically performed within 600 s. The plate was kept at the reaction temperature and shaken for another 600 s after the addition. 30 μ L of each 500 μ L final reaction solution were removed, diluted with 270 μ L dodecane and placed into a 96-well Hellma quartz microreader plate. A Biotek Synergy 4 microplate reader was used to evaluate the reaction solutions. An automatic calibration was carried out before each plate was measured, then absorption spectra were recorded from 200 to 500 nm in 1 nm increments with a single reading per data point, while emission spectra were recorded from 350 - 500 nm in 1 nm increments with an excitation wavelength of 315 nm, a detector sensitivity of 70 and a single reading per data point.

Acknowledgements

The authors gratefully acknowledge Y. Cho for providing results of exciton energy calculations of magic sized nanosheets. J.C.D and J.J.C acknowledge funding through the NSF-GRFP program under DGE 1752814, and J.C.D, E.C and J.J.C acknowledge funding from the Kavli NanoScience Institute, University of California, Berkeley through the Philomathia Graduate Student Fellowship. Work at the Molecular Foundry was supported by the Office of Science, Office of Basic Energy Sciences, of the U.S. Department of Energy under Contract No. DE-AC02-05CH11231. Other work reported here was supported by the U.S. Department of Energy, Office of Science, Office of Basic Energy Sciences, Materials Sciences and Engineering Division, under Contract No. DE-AC02-05-CH11231 within the Physical Chemistry of Inorganic Nanostructures Program (KC3103). M.L and M.H.-G. acknowledge funding by the U.S. Department of Energy, Office of Science, Office of Advanced Scientific Computing, and Office of Basic Energy Sciences, via the Scientific Discovery through Advanced Computing (SciDAC) program.

References

1. Jena, A. K.; Kulkarni, A.; Miyasaka, T. Halide Perovskite Photovoltaics: Background, Status, and Future Prospects. *Chemical Reviews* **2019**, *119*, 3036–3103.

2. Lu, M.; Zhang, Y.; Wang, S.; Guo, J.; Yu, W. W.; Rogach, A. L. Metal Halide Perovskite Light-Emitting Devices: Promising Technology for Next-Generation Displays. *Advanced Functional Materials* **2019**, *29*, 1902008.

3. Yakunin, S.; Protesescu, L.; Krieg, F.; Bodnarchuk, M. I.; Nedelcu, G.; Humer, M.; De Luca, G.; Fiebig, M.; Heiss, W.; Kovalenko, M. V. Low-threshold amplified spontaneous emission and lasing from colloidal nanocrystals of caesium lead halide perovskites. *Nature Communications* **2015**, *6*, 8056.

4. Zhao, Y.; Zhu, K. Organic–inorganic hybrid lead halide perovskites for optoelectronic and electronic applications. *Chemical Society Reviews* **2016**, *45*, 655–689.

5. Koscher, B. A.; Bronstein, N. D.; Olshansky, J. H.; Bekenstein, Y.; Alivisatos, A. P. Surface- vs Diffusion-Limited Mechanisms of Anion Exchange in CsPbBr3 Nanocrystal Cubes Revealed through Kinetic Studies. *Journal of the American Chemical Society* **2016**, *138*, 12065–12068.

6. Imran, M.; Ijaz, P.; Baranov, D.; Goldoni, L.; Petralanda, U.; Akkerman, Q.; Abdelhady, A. L.; Prato, M.; Bianchini, P.; Infante, I.; Manna, L. Shape-Pure, Nearly Monodispersed CsPbBr 3 Nanocubes Prepared Using Secondary Aliphatic Amines. *Nano Letters* **2018**, *18*, 7822–7831.

7. Utzat, H.; Sun, W.; Kaplan, A. E. K.; Krieg, F.; Ginterseder, M.; Spokoyny, B.; Klein, N. D.; Shulenberger, K. E.; Perkinson, C. F.; Kovalenko, M. V.; Bawendi, M. G. Coherent single-photon emission from colloidal lead halide perovskite quantum dots. *Science* **2019**, *363*, 1068–1072.

8. Rainò, G.; Becker, M. A.; Bodnarchuk, M. I.; Mahrt, R. F.; Kovalenko, M. V.; Stöferle, T. Superfluorescence from lead halide perovskite quantum dot superlattices. *Nature* **2018**, *563*, 671–675.

9. Pradhan, N. Growth of Lead Halide Perovskite Nanocrystals: Still in Mystery. *ACS Physical Chemistry Au* **2022**, acsphyschemau.2c00001.

10. Owen, J. S.; Park, J.; Trudeau, P.-E.; Alivisatos, A. P. Reaction Chemistry and Ligand Exchange at Cadmium-Selenide Nanocrystal Surfaces. *Journal of the American Chemical Society* **2008**, *130*, 12279–12281.

11. Owen, J. S.; Chan, E. M.; Liu, H.; Alivisatos, A. P. Precursor Conversion Kinetics and the Nucleation of Cadmium Selenide Nanocrystals. *Journal of the American Chemical Society* **2010**, *132*, 18206–18213.

12. Rodrigues, T. S.; Zhao, M.; Yang, T.; Gilroy, K. D.; da Silva, A. G. M.; Camargo, P. H. C.; Xia, Y. Synthesis of Colloidal Metal Nanocrystals: A Comprehensive Review on the Reductants. *Chemistry – A European Journal* **2018**, *24*, 16944–16963.

13. Gary, D. C.; Terban, M. W.; Billinge, S. J. L.; Cossairt, B. M. Two-Step Nucleation and Growth of InP Quantum Dots via Magic-Sized Cluster Intermediates. *Chemistry of Materials* **2015**, *27*, 1432–1441.

14. Hendricks, M. P.; Campos, M. P.; Cleveland, G. T.; Jen-La Plante, I.; Owen, J. S. A tunable library of substituted thiourea precursors to metal sulfide nanocrystals. *Science* **2015**, *348*, 1226–1230.

15. Protesescu, L.; Yakunin, S.; Bodnarchuk, M. I.; Krieg, F.; Caputo, R.; Hendon, C. H.; Yang, R. X.; Walsh, A.; Kovalenko, M. V. Nanocrystals of Cesium Lead Halide Perovskites (CsPbX3, X = Cl, Br, and I): Novel Optoelectronic Materials Showing Bright Emission with Wide Color Gamut. *Nano Letters* **2015**, *15*, 3692–3696.

16. Murray, C. B.; Norris, D. J.; Bawendi, M. G. Synthesis and characterization of nearly monodisperse CdE (E = sulfur, selenium, tellurium) semiconductor nanocrystallites. *Journal of the American Chemical Society* **1993**, *115*, 8706–8715.

17. Liu, Z.; Bekenstein, Y.; Ye, X.; Nguyen, S. C.; Swabeck, J.; Zhang, D.; Lee, S. T.; Yang, P.; Ma, W.; Alivisatos, A. P. Ligand Mediated Transformation of Cesium Lead Bromide Perovskite Nanocrystals to Lead Depleted Cs4PbBr6 Nanocrystals. *Journal of the American Chemical Society* **2017**, *139*, 5309–5312.

18. Palazon, F.; Urso, C.; De Trizio, L.; Akkerman, Q.; Marras, S.; Locardi, F.; Nelli, I.; Ferretti, M.; Prato, M.; Manna, L. Postsynthesis Transformation of Insulating Cs 4 PbBr 6 Nanocrystals into Bright Perovskite CsPbBr 3 through Physical and Chemical Extraction of CsBr. *ACS Energy Letters* **2017**, *2*, 2445–2448.

19. Udayabhaskararao, T.; Kazes, M.; Houben, L.; Lin, H.; Oron, D. Nucleation, Growth, and Structural Transformations of Perovskite Nanocrystals. *Chemistry of Materials* **2017**, *29*, 1302–1308.

20. Dahl, J. C.; Wang, X.; Huang, X.; Chan, E. M.; Alivisatos, A. P. Elucidating the Weakly Reversible Cs–Pb–Br Perovskite Nanocrystal Reaction Network with High-Throughput Maps and Transformations. *Journal of the American Chemical Society* **2020**, *142*, 11915–11926.

21. Imran, M.; Caligiuri, V.; Wang, M.; Goldoni, L.; Prato, M.; Krahne, R.; De Trizio, L.; Manna, L. Benzoyl Halides as Alternative Precursors for the Colloidal Synthesis of Lead-Based Halide Perovskite Nanocrystals. *Journal of the American Chemical Society* **2018**, *140*, 2656–2664.

22. Dahl, J. C.; Osowiecki, W. T.; Cai, Y.; Swabeck, J. K.; Bekenstein, Y.; Asta, M.; Chan, E. M.; Alivisatos, A. P. Probing the Stability and Band Gaps of Cs 2 AgInCl 6 and Cs 2 AgSbCl 6 Lead-Free Double Perovskite Nanocrystals. *Chemistry of Materials* **2019**, *31*, 3134–3143.

23. Zhang, Z.; Skripka, A.; Dahl, J. C.; Dun, C.; Urban, J. J.; Jaque, D.; Schuck, P. J.; Cohen, B. E.; Chan, E. M. Tuning Phonon Energies in Lanthanide-doped Potassium Lead Halide Nanocrystals for Enhanced Nonlinearity and Upconversion. *Angewandte Chemie International Edition* **2023**, *62*, e202212549.

24. Creutz, S. E.; Crites, E. N.; De Siena, M. C.; Gamelin, D. R. Colloidal Nanocrystals of Lead-Free Double-Perovskite (Elpasolite) Semiconductors: Synthesis and Anion Exchange to Access New Materials. *Nano Letters* **2018**, *18*, 1118–1123.

25. Bekenstein, Y.; Dahl, J. C.; Huang, J.; Osowiecki, W. T.; Swabeck, J. K.; Chan, E. M.; Yang, P.; Alivisatos, A. P. The Making and Breaking of Lead-Free Double Perovskite

Nanocrystals of Cesium Silver-Bismuth Halide Compositions. *Nano Letters* **2018**, *18*, 3502–3508.

26. Wen, J.-R.; Roman, B. J.; Rodriguez Ortiz, F. A.; Mireles Villegas, N.; Porcellino, N.; Sheldon, M. Chemical Availability of Bromide Dictates CsPbBr 3 Nanocrystal Growth. *Chemistry of Materials* **2019**, *31*, 8551–8557.

27. Bera, S.; Behera, R. K.; Pradhan, N. alpha-Halo Ketone for Polyhedral Perovskite Nanocrystals: Evolutions, Shape Conversions, Ligand Chemistry, and Self-Assembly. *Journal of the American Chemical Society* **2020**, *142*, 20865–20874.

28. Li, F.; Lin, F.; Huang, Y.; Cai, Z.; Qiu, L.; Zhu, Y.; Jiang, Y.; Wang, Y.; Chen, X. Bromobenzene aliphatic nucleophilic substitution guided controllable and reproducible synthesis of high quality cesium lead bromide perovskite nanocrystals. *Inorganic Chemistry Frontiers* **2019**, *6*, 3577–3582.

29. Parr, R. G.; Pearson, R. G. Absolute hardness: companion parameter to absolute electronegativity. *Journal of the American Chemical Society* **1983**, *105*, 7512–7516.

30. Ferri, D.; Salvatore, F.; Vasca, E. Complex Formation Between Lead(II) and Bromide Ions. *Journal of Coordination Chemistry* **1989**, *20*, 11–20.

31. Jones, A.; Aikens, D. The nature of pb(II)-bromide complexes in propylene carbonate. *Polyhedron* **1982**, *1*, 169–174.

32. Dahl, J. C.; Niblett, S.; Cho, Y.; Wang, X.; Zhang, Y.; Chan, E. M.; Alivisatos, A. P. Scientific Machine Learning of 2D Perovskite Nanosheet Formation. *Journal of the American Chemical Society* **2023**, *145*, 23076–23087.

33. Hassan, Y.; Song, Y.; Pensack, R. D.; Abdelrahman, A. I.; Kobayashi, Y.; Winnik, M. A.; Scholes, G. D. Structure-Tuned Lead Halide Perovskite Nanocrystals. *Advanced Materials* **2016**, *28*, 566–573.

34. Peng, Z. A.; Peng, X. Nearly Monodisperse and Shape-Controlled CdSe Nanocrystals via Alternative Routes: Nucleation and Growth. *Journal of the American Chemical Society* **2002**, *124*, 3343–3353.

35. Liu, S.; Yu, Q.; Zhang, C.; Zhang, M.; Rowell, N.; Fan, H.; Huang, W.; Yu, K.; Liang, B. Transformation of ZnS Precursor Compounds to Magic-Size Clusters Exhibiting Optical Absorption Peaking at 269 nm. *The Journal of Physical Chemistry Letters* **2020**, *11*, 75–82.

36. Zhang, B.; Altamura, D.; Caliandro, R.; Giannini, C.; Peng, L.; De Trizio, L.; Manna, L. Stable CsPbBr3 Nanoclusters Feature a Disk-like Shape and a Distorted Orthorhombic Structure. *Journal of the American Chemical Society* **2022**, *144*, 5059–5066.

37. Hamachi, L. S.; Yang, H.; Jen-La Plante, I.; Saenz, N.; Qian, K.; Campos, M. P.; Cleveland, G. T.; Rreza, I.; Oza, A.; Walravens, W.; Chan, E. M.; Hens, Z.; Crowther, A. C.; Owen, J. S. Precursor reaction kinetics control compositional grading and size of CdSe 1-x S x nanocrystal heterostructures. *Chemical Science* **2019**, *10*, 6539–6552.

38. Oldenburg, K.; Vogler, A. Electronic Spectra and Photochemistry of Tin(II), Lead(II), Antimony(III), and Bismuth(III) Bromide Complexes in Solution. *Zeitschrift für Naturforschung B* **1993**, *48*, 1519–1523.

39. Yoon, S. J.; Stamplecoskie, K. G.; Kamat, P. V. How Lead Halide Complex Chemistry Dictates the Composition of Mixed Halide Perovskites. *Journal of Physical Chemistry Letters* **2016**, *7*, 1368–1373.

40. Horváth, O.; Marosvölgyi, T.; Vörös, J. *From Colloids to Nanotechnology*; Springer Berlin Heidelberg: Berlin, Heidelberg, 2004; pp 17–23.

41. Sharenko, A.; Mackeen, C.; Jewell, L.; Bridges, F.; Toney, M. F. Evolution of Iodoplumbate Complexes in Methylammonium Lead Iodide Perovskite Precursor Solutions. *Chemistry of Materials* **2017**, *29*, 1315–1320.

42. Guo, Y.; Shoyama, K.; Sato, W.; Matsuo, Y.; Inoue, K.; Harano, K.; Liu, C.; Tanaka, H.; Nakamura, E. Chemical Pathways Connecting Lead(II) Iodide and Perovskite via Polymeric Plumbate(II) Fiber. *Journal of the American Chemical Society* **2015**, *137*, 15907–15914.

43. Hao, F.; Stoumpos, C. C.; Liu, Z.; Chang, R. P. H.; Kanatzidis, M. G. Controllable Perovskite Crystallization at a Gas–Solid Interface for Hole Conductor-Free Solar Cells with Steady Power Conversion Efficiency over 10%. *Journal of the American Chemical Society* **2014**, *136*, 16411–16419.

44. Wakamiya, A.; Endo, M.; Sasamori, T.; Tokitoh, N.; Ogomi, Y.; Hayase, S.; Murata, Y. Reproducible Fabrication of Efficient Perovskite-based Solar Cells: X-ray Crystallographic Studies on the Formation of CH 3 NH 3 PbI 3 Layers. *Chemistry Letters* **2014**, *43*, 711–713.

45. Fateev, S. A.; Petrov, A. A.; Khrustalev, V. N.; Dorovatovskii, P. V.; Zubavichus, Y. V.; Goodilin, E. A.; Tarasov, A. B. Solution Processing of Methylammonium Lead Iodide Perovskite from γ-Butyrolactone: Crystallization Mediated by Solvation Equilibrium. *Chemistry of Materials* **2018**, *30*, 5237–5244.

46. Riedinger, A.; Ott, F. D.; Mule, A.; Mazzotti, S.; Knüsel, P. N.; Kress, S. J.; Prins, F.; Erwin, S. C.; Norris, D. J. An intrinsic growth instability in isotropic materials leads to quasi-two-dimensional nanoplatelets. *Nature Materials* **2017**, *16*, 743–748.

47. Ott, F. D.; Riedinger, A.; Ochsenbein, D. R.; Knüsel, P. N.; Erwin, S. C.; Mazzotti, M.; Norris, D. J. Ripening of Semiconductor Nanoplatelets. *Nano Letters* **2017**, *17*, 6870–6877.

48. Knüsel, P. N.; Riedinger, A.; Rossinelli, A. A.; Ott, F. D.; Mule, A. S.; Norris, D. J. Experimental Evidence for Two-Dimensional Ostwald Ripening in Semiconductor Nanoplatelets. *Chemistry of Materials* **2020**, *32*, 3312–3319.

49. Akkerman, Q. A.; Nguyen, T. P.; Boehme, S. C.; Montanarella, F.; Dirin, D. N.; Wechsler, P.; Beiglböck, F.; Rainò, G.; Erni, R.; Katan, C.; Even, J.; Kovalenko, M. V. Controlling the nucleation and growth kinetics of lead halide perovskite quantum dots. *Science* **2022**, *377*, 1406–1412.

50. Montanarella, F.; Akkerman, Q. A.; Bonatz, D.; van der Sluijs, M. M.; van der Bok, J. C.; Prins, P. T.; Aebli, M.; Mews, A.; Vanmaekelbergh, D.; Kovalenko, M. V. Growth and Self-Assembly of CsPbBr3 Nanocrystals in the TOPO/PbBr2 Synthesis as Seen with X-ray Scattering. *Nano Letters* **2023**, *23*, 667–676.

51. Lu, C.; Wright, M. W.; Ma, X.; Li, H.; Itanze, D. S.; Carter, J. A.; Hewitt, C. A.; Donati, G. L.; Carroll, D. L.; Lundin, P. M.; Geyer, S. M. Cesium Oleate Precursor Preparation for Lead Halide Perovskite Nanocrystal Synthesis: The Influence of Excess Oleic Acid on Achieving Solubility, Conversion, and Reproducibility. *Chemistry of Materials* **2019**, *31*, 62–67.

52. Epifanovsky, E.; Gilbert, A. T.; Feng, X.; Lee, J.; Mao, Y.; Mardirossian, N.; Pokhilko, P.; White, A. F.; Coons, M. P.; Dempwolff, A. L.; Gan, Z.; Hait, D.; Horn, P. R.; Jacobson, L. D.; Kaliman, I.; Kussmann, J.; Lange, A. W.; Lao, K. U.; Levine, D. S.; Liu, J. *et al.* Software for the frontiers of quantum chemistry: An overview of developments in the Q-Chem 5 package. *Journal of Chemical Physics* **2021**, *155*, 084801.

53. Becke, A. D. Density-functional exchange-energy approximation with correct asymptotic behavior. *Physical Review A* **1988**, *38*, 3098–3100.

54. Lee, C.; Yang, W.; Parr, R. G. Development of the Colle-Salvetti correlation-energy formula into a functional of the electron density. *Physical Review B* **1988**, *37*, 785–789.

55. Becke, A. D. Density-functional thermochemistry. III. The role of exact exchange. *The Journal of Chemical Physics* **1993**, *98*, 5648–5652.

56. Rappoport, D.; Furche, F. Property-optimized Gaussian basis sets for molecular response calculations. *The Journal of Chemical Physics* **2010**, *133*, 134105.

57. Weigend, F.; Ahlrichs, R. Balanced basis sets of split valence, triple zeta valence and quadruple zeta valence quality for H to Rn: Design and assessment of accuracy. *Physical Chemistry Chemical Physics* **2005**, *7*, 3297.

58. Andrae, D.; Huermann, U.; Dolg, M.; Stoll, H.; Preu, H. Energy-adjustedab initio pseudopotentials for the second and third row transition elements. *Theoretica Chimica Acta* **1990**, *77*, 123–141.

59. Grimme, S. Density functional theory with London dispersion corrections. *WIREs Computational Molecular Science* **2011**, *1*, 211–228.

60. Marenich, A. V.; Cramer, C. J.; Truhlar, D. G. Universal Solvation Model Based on the Generalized Born Approximation with Asymmetric Descreening. *Journal of Chemical Theory and Computation* **2009**, *5*, 2447–2464.

61. Dahlgren, B. ChemPy: A package useful for chemistry written in Python. *Journal of Open Source Software* **2018**, *3*, 565.

TOC Graphic

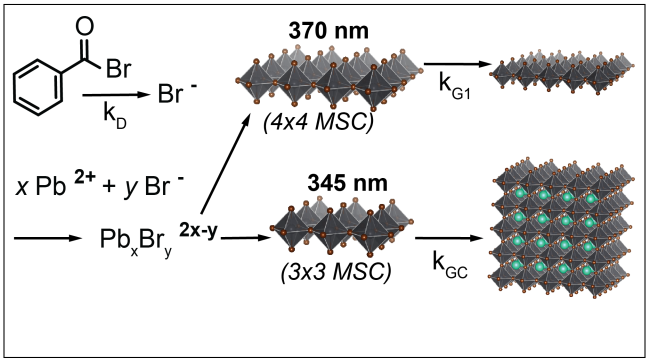
370 nm
Br
$\xrightarrow{k_D}$ Br $^-$
(4x4 MSC)
k_{G1}
x Pb $^{2+}$ + y Br $^-$
$\longrightarrow$ $Pb_xBr_y^{2x-y}$
345 nm
(3x3 MSC)
k_{GC}